Theoretical study of differential charge-transfer cross sections for $Ne^{4+}+He$ collisions at low energies

J. Tan* and C. D. Lin
Department of Physics, Kansas State University, Manhattan, Kansas 66506
(Received 27 August 1987)

A quantal two-channel calculation is applied to study charge-transfer differential cross sections in Ne^{4+} on He collisions at laboratory impact energies from 220 to 500 eV. The experimental data of Tunnell *et al.* were used to fit empirical potential curves and coupling terms from which the observed oscillatory structures in the differential cross sections were analyzed. In contrast with the double-charge-transfer process in C^{4+} on He, where the oscillations in the differential cross sections are attributed to pure Stueckelberg oscillations, we demonstrated that the differential cross sections for charge transfer in Ne^{4+} on He exhibit many fine fast oscillations and the observed structures are due to the envelopes of these unresolved fast oscillations. Classical deflection functions are used to help in interpreting the calculated oscillations.

I. INTRODUCTION

Differential scattering cross sections in atom-atom and in ion-atom collisions provide detailed information about the interaction potentials between the two collision partners. For atom-atom collisions and collisions of singly charged ions with neutral atoms, a considerable volume of experimental measurements and some theoretical analysis have been made since the 1970s.[1-6] With the availability of low-velocity multiply charged ions in recent years, measurements of differential cross sections in charge-transfer processes of these ions with atoms have now been reported[7-9] for a number of collision systems.

In the collisions between multiply charged ions with atoms, often there are many projectile excited levels populated through charge-transfer reactions. In selective systems, however, there will be only one dominant charge-transfer channel for collisions at low energies. Experimentally, this can be confirmed via energy-gain spectroscopy. For such simple collision systems, a detailed theoretical analysis becomes possible. Information about the collision system can be further refined through the investigation of differential cross sections.

The differential scattering patterns, in most cases, show oscillating features of several types, some of them are due to the semiclassical rainbow scattering or glory scattering;[1] others can be related semiclassically to the existence of two or more trajectories resulting in scattering at the same observed angle and at the same final velocity.[2] In a previous study,[10] we have shown that the observed oscillatory features in the double-charge-transfer differential cross sections in C^{4+} on He collisions can be attributed to "pure" Stueckelberg oscillations, i.e., the oscillations are due to the interference between two paths leading to the final double-capture channel.

Experimental differential cross-section measurements by Tunnell *et al.*[7] on a "similar" collision system, Ne^{4+} on He, showed that their oscillatory structures exhibit different features from those shown for the C^{4+} on He system.[9] Furthermore, experimental energy-gain spectroscopy indicated that for collision energy in the range of 220–500 eV, the dominant inelastic process is

$$Ne^{4+}(2p^2,{}^3P)+He(1s^2) \rightarrow Ne^{3+}(2p^2 3s,{}^{2,4}P)+He^{+}(1s)\ , \quad (1)$$

such that the collision can be approximated as a two-channel scattering system (if we neglect the doublet and quartet splittings). Thus it is desirable to understand the origin of the different oscillatory features in the two collision systems.

In the lack of reliable *ab initio* potential curves and coupling terms for the Ne^{4+} on He system, we rely in our analysis on fitting potential curves and coupling terms so that a quantal calculation based on these empirical potentials can reproduce the measured differential cross sections of Tunnell *et al.* We first note that the crossing radius $R_\times$ for the two relevant potential curves occurs at a much larger internuclear separation (7.1 a.u.) for the present system where one of the curves is attractive and the other is repulsive. In contrast, for the C^{4+} on He system, the crossing radius is small (3.1 a.u.) and the two potentials inside $R_\times$ are both steep repulsive curves. Thus, although both systems exhibit oscillatory structures in the differential cross sections, the theoretical interpretations are quite different. In this paper we conclude that the experimental oscillatory features for Ne^{4+} on He are due to the envelopes of the unresolved (in angles) fast Stueckelberg oscillations. When these theoretical differential cross sections are folded with experimental angular resolutions, good agreement with experimental data is achieved. To understand the different features of the oscillations, a semiclassical analysis in terms of deflection functions is also presented.

The rest of this paper is organized as follows. In Sec. II, we review the quantal formulation of heavy-particle scattering in the adiabatic or diabatic molecular basis and the solution of the scattering equations. In Sec.

III A, we discuss the procedure for obtaining semiempirical potential curves and the coupling terms for Ne^{4+} on He, using C^{4+} on He as guidance. In Sec. III B the differential cross sections calculated from the fitted empirical potential curves are compared with experimental measurements at several energies. To understand the oscillatory features, the deflection functions are calculated in Sec. III C and compared with those for C^{4+} on He to explain the origin of the different oscillations. A short summary is given in Sec. IV. Atomic units are used throughout unless otherwise specified.

II. REVIEW OF THE QUANTUM FORMULATION OF ION-ATOM COLLISIONS

The Hamiltonian of a scattering system consisting of an ion and a neutral atom in the center-of-mass (c.m.) frame is

$$H=\left[-\frac{1}{2\mu}\nabla_{\mathbf{R}}^2+\frac{Z_I Z_A}{R}\right]+\left[-\frac{1}{2m}\nabla_{\mathbf{r}}^2+V(R,\mathbf{r})\right]$$
$$=H_N+H_e\ , \tag{2}$$

where H_N and H_e are the nuclear and the electronic Hamiltonians, respectively, $\mathbf{r}$ stands for the coordinates of all the collisionally active electrons, R is the internuclear separation, μ is the reduced mass of the two nuclei, and m ($\simeq 1$) is the reduced mass of the electron in the system; Z_I and Z_A are the charges of the ion and of the atomic core, respectively.

Within the perturbed stationary-state approximation for slow collisions, the heavy particle with mass μ is regarded as being scattered by an effective potential which consists of many discrete energy surfaces, namely, the Hamiltonian for the heavy particle is

$$H=-\frac{1}{2\mu}\nabla_{\mathbf{R}}^2+V_{\text{eff}}\ . \tag{3}$$

The potential surfaces V_{eff} are the sum of the Coulomb repulsion $Z_I Z_A/R$ between the two nuclei and the electronic eigenvalues, $E_n(R)$, obtained by solving the electronic Hamiltonian at each fixed R:

$$H_e(R,\mathbf{r})\Phi_n(R;\mathbf{r})=E_n(R)\Phi_n(R;\mathbf{r})\ . \tag{4}$$

These energy surfaces, $E_n(R)+Z_I Z_A/R$, are the adiabatic potentials.

If the total wave function is expanded in the adiabatic basis,

$$\bar{\Psi}(\mathbf{R},\mathbf{r})=\sum_n F_n^a(\mathbf{R})\Phi_n(R;\mathbf{r})\ , \tag{5}$$

the motion of the heavy particle is governed by the differential equation

$$\left[-\frac{1}{2\mu}(\nabla_{\mathbf{R}}\underline{I}+\underline{P})^2+\underline{V}^a-E\underline{I}\right]\mathbf{F}^a(\mathbf{R})=\mathbf{0}\ , \tag{6}$$

where the potential matrix is diagonal, $V_{nm}=[E_n(R)+Z_I Z_A/R]\delta_{nm}$, and the off-diagonal elements of the Hamiltonian are the nonadiabatic couplings, $P_{nm}=\langle\Phi_n\,|\,\nabla_{\mathbf{R}}\,|\,\Phi_m\rangle$.

The second-order differential equations (6) contain first-order derivatives. From the numerical computational viewpoint, it is more convenient to transform the equations to the diabatic representation such that the wave function of the heavy particle is $\mathbf{F}^d=\underline{C}^{-1}\mathbf{F}^a$ where the unitary transformation matrix $\underline{C}$ satisfies

$$d\underline{C}/dR+\underline{P}\,\underline{C}=\underline{0}\ . \tag{7}$$

In (7), we consider radial coupling only. The boundary condition for $\underline{C}$ is

$$\underline{C}(R)\rightarrow\underline{I}\ \text{ as } R\rightarrow\infty\ . \tag{8}$$

For two-channel systems, the transformation matrix can be written as

$$\underline{C}(R)=\begin{bmatrix}\cos\varepsilon(R) & \sin\varepsilon(R)\\ -\sin\varepsilon(R) & \cos\varepsilon(R)\end{bmatrix}, \tag{9}$$

where the transformation angle is

$$\varepsilon(R)=\int_R^\infty P_{12}(R')dR'\ . \tag{10}$$

In the diabatic representation, $\mathbf{F}^d$ now satisfies

$$\left[-\frac{1}{2\mu}\nabla_{\mathbf{R}}^2\underline{I}+\underline{V}^d(R)-E\underline{I}\right]\mathbf{F}^d(\mathbf{R})=\mathbf{0}\ , \tag{11}$$

where the diabatic potential matrix $\underline{V}^d=\underline{C}^{-1}\underline{V}^a\underline{C}$ has nonzero off-diagonal matrix elements.

The partial differential equation (11) can be solved by expanding into partial waves,[4]

$$\mathbf{F}^d(\mathbf{R})=\sum_{L,M}(-1)^L\left[\frac{2L+1}{4\pi}\right]^{1/2}D^L_{\Lambda M}(\hat{\mathbf{R}})\frac{\mathbf{f}^L(R)}{R}\ , \tag{12}$$

where L is the total angular momentum of the whole collision system, M is its projection along the laboratory axis, Λ is the projection of the electronic angular momentum along the internuclear axis, and $D^L_{\Lambda M}$ is the usual rotation matrix. The radial partial wave functions $\mathbf{f}^L(R)$ satisfy for each L the coupled differential equations

$$\left[-\frac{1}{2\mu}\left[\frac{d^2}{dR^2}-\frac{L(L+1)-\Lambda^2}{R^2}\right]\underline{I}+\underline{V}^d(R)-E\underline{I}\right]$$
$$\times\mathbf{f}^L(R)=\mathbf{0}\ . \tag{13}$$

In calculations considered here, $M=0$ because of the cylindrical symmetry of the scattering. Under the two-channel approximation, (13) reduces to a set of two coupled differential equations. Each set of equations is solved numerically using the log-derivative method of Johnson[11] to obtain the asymptotic scattering wave functions $\mathbf{f}^L(R)$ from which the scattering matrix S is obtained.

The S matrix calculated is used to evaluate the differential cross sections and to extract information such as the semiclassical deflection functions for a more detailed understanding of the collision system.

III. APPLICATIONS TO THE SCATTERING SYSTEM $Ne^{4+}+He$

A. Modeling of scattering potentials and coupling terms

In this work we do not attempt to obtain the *ab initio* potential curves for the $Ne^{4+}+He$ system, instead we model the potentials with the aid of experimental differential cross-section data. For reasons to be explained later, the construction of the model potentials starts from the adiabatic representation. Let the potentials be $E_1(R)$ and $E_2(R)$, for the elastic and the charge-transfer channel, respectively. In the limit of $R\rightarrow\infty$, they are equal to the separated-atom energies. From the atomic binding energies (or the Q-value measurements) we know that E_2 is 0.46 a.u. lower than E_1 in this limit. Furthermore, at large R, $E_1(R)$ is given by the polarization potential $-\alpha Z_I^2/2R^4$, where $\alpha=1.28$ is the polarizability of helium and $Z_I=4$ for Ne^{4+}. For the charge-transfer channel, asymptotically $E_2(R)$ is given by $(Z_I-1)/R$, the Coulomb repulsion between Ne^{3+} and He^+. At small internuclear separations, both potentials are dominated by the Coulomb repulsion Z_IZ_A/R so that the behavior of $E_n(R)$ in this region is not important. From the knowledge of the potentials in these two limits, we can smoothly join the small-R region to the large-R region. The nonadiabatic coupling term $P_{12}(R)$ is chosen to be a Gaussian form. It was found that the calculated differential cross sections do not depend on the width or height of the function significantly. We thus finally used the P_{12} from the C^{4+} on He system in the present calculation. The energy separation at the crossing point is adjusted until the calculated differential cross sections resemble the experimental data.

The empirical adiabatic and diabatic potentials used in the final analysis are shown in Fig. 1(a). Details in the crossing region are shown in the inset. In Fig. 1(b) the coupling terms and the transformation angle are displayed.

B. The differential cross sections

In the c.m. frame the differential cross section for a particle with incident momentum k_1, scattered with momentum k_2 at angle θ with respect to the incident direction is given by

$$\sigma(\theta)=2\pi\frac{k_2}{k_1}\sin\theta\,|f(\theta)|^2\,, \tag{14}$$

where the scattering amplitude is

$$f(\theta)=\frac{1}{2i\sqrt{k_1k_2}}\sum_L(2L+1)S_{12}^L P_L(\cos\theta)\,. \tag{15}$$

In (15), S_{12}^L is the scattering matrix element for charge transfer and P_L is the Legendre polynomial of order L. In the actual calculation, partial waves from $L=400$ to 1300 are included in the summation to achieve converged results.

The quantal differential cross sections calculated from our fitted potentials are shown in Fig. 2(a) at the labora-

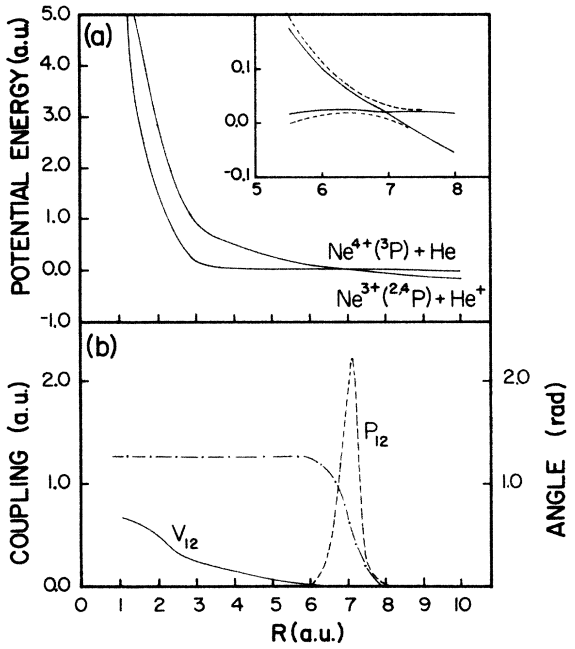

FIG. 1. (a) Adiabatic and diabatic potential surfaces of $(NeHe)^{4+}$. The solid curves represent the diabatic potential surfaces. The dashed curves on the upper right corner are the adiabatic potentials. (b) Channel couplings: V_{12} (solid line) and P_{12} (dashed line). The dash-dotted line is the diabatic transformation angle ε (the scale is referred to the right vertical axis).

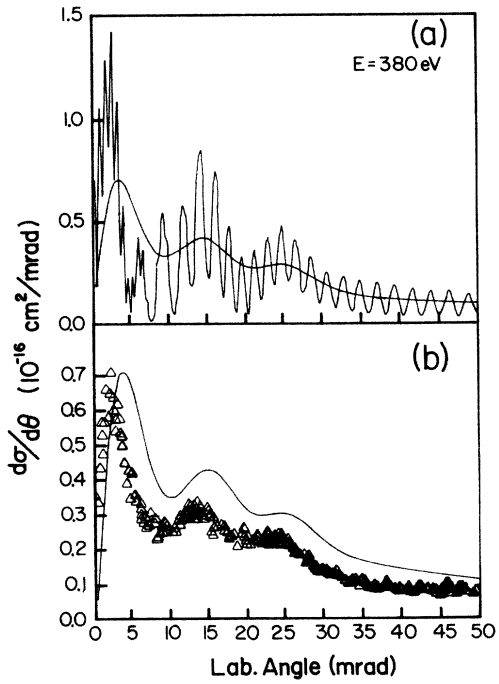

FIG. 2. (a) Quantal result of differential charge-transfer cross section for $Ne^{4+}+He$ at $E_{lab}=380$ eV. (b) Comparison of experimental data (Ref. 7) with theoretical results folded with experimental angular resolution (4.8 mrad).

tory impact energy 380 eV. In Fig. 2(b) the theoretical calculations are convoluted with experimental angular resolutions (4.8 mrad) and are compared with the experimental data from Tunnell *et al.*[7] We note that the oscillatory structures in the experimental data are due to the oscillation in the envelope in the theoretical calculation. The fast fine oscillations in the calculation can be tested only with a better angular resolution.

The theoretical cross sections are somewhat higher than the experimental data. A better agreement can be obtained by reducing the magnitude of the coupling strength P_{12}. This is not the main goal of this work. Instead, we point out that there are clearly three types of oscillations in the calculated curve shown in Fig. 2(a); the fast oscillations on top of the forward peaking, the Stueckelberg oscillations, and the slow oscillations which comprise the experimental observed structures. This is different from the oscillatory structure in the double-charge-transfer differential cross sections in C^{4+} on helium collisions studied previously. In the latter case, the structure is due to pure Stueckelberg oscillations. Our main goal is to interpret the differences. This is achieved with the aid of the semiclassical deflection function which is given in Sec. III C.

We have applied the same model potentials to study the collisions at several energies from 220 to 484 eV. The theoretical calculations and the results of convolutions with experimental angular resolutions are displayed

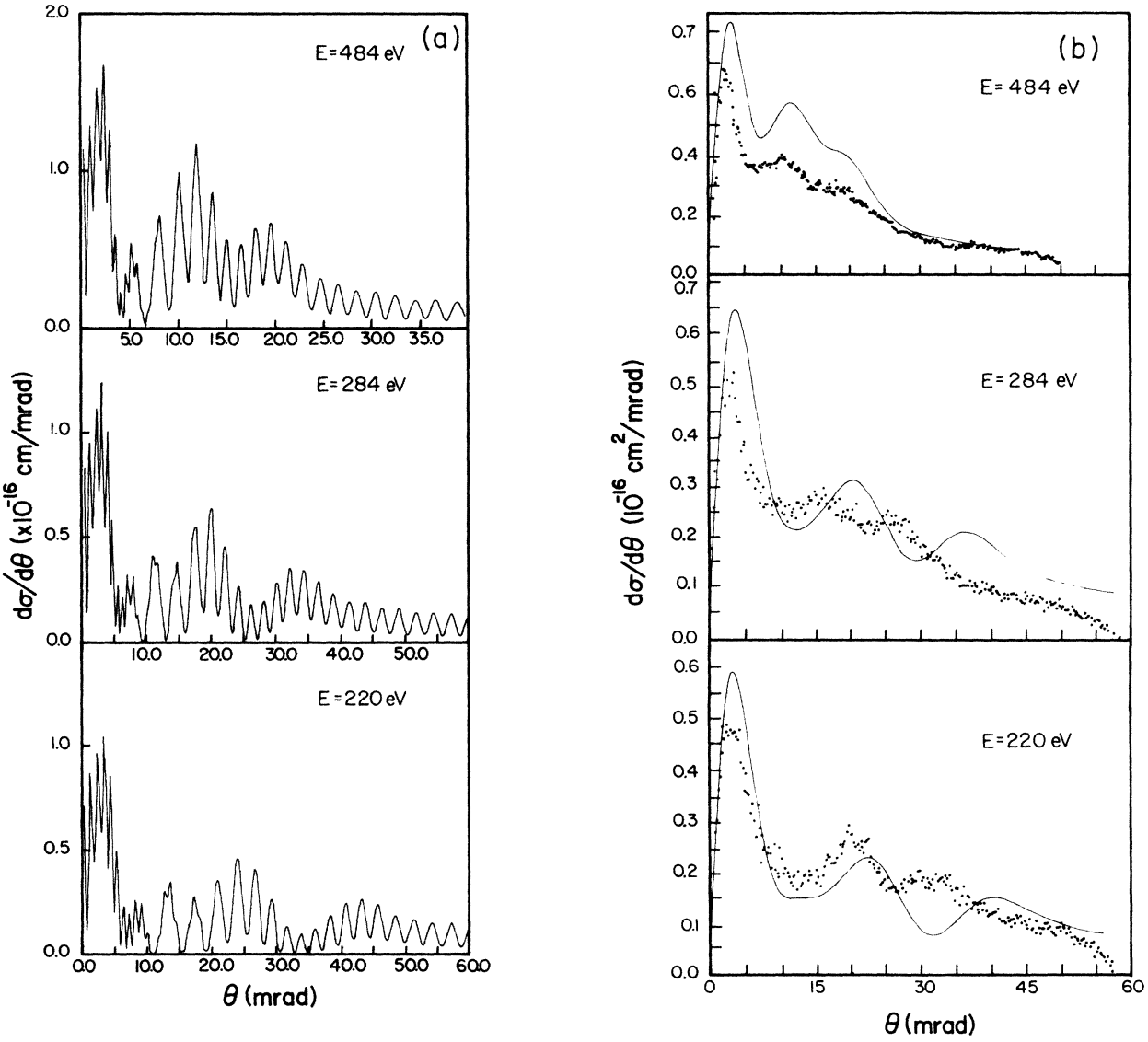

FIG. 3. Differential charge-transfer cross sections of $Ne^{4+}+He$ at laboratory impact energies from 484 to 220 eV. (a) Quantal calculation; (b) experimental data taken from Ref. 7, and theoretical calculations folded with experimental angular resolutions.

on Fig. 3. The agreement is quite satisfactory except for the lowest energy where one expects that the theoretical result is more sensitive to the potentials used.

C. The deflection function

The number of partial waves contributing to the sum in (15) is quite large. The sum can be evaluated using the stationary-phase approximation. For large L and $L\theta \gg 1$, we have

$$P_L(\cos\theta)=\left[\frac{2}{(L+\frac{1}{2})\pi\sin\theta}\right]^{1/2} \times\sin[(L+\tfrac{1}{2})\theta+\pi/4] \tag{16}$$

which is oscillatory. The matrix element S_{12} (considered as a function of L) is also oscillatory, we can express it as

$$S_{12}=A\sin\xi\exp(i\eta_{12}) , \\ =A\frac{1}{2i}\{\exp[i(\eta_{12}+\xi)]-\exp[i(\eta_{12}-\xi)]\} , \tag{17}$$

where the envelope A is a slow-varying function of L. The L integration in (15) of these oscillatory functions gives a negligible contribution to the differential cross section $\sigma(\theta)$ except at points of stationary phases. These stationary phases are determined at the points where the derivative of the total phase of the products with respect to L is zero. An analysis based on the stationary-phase approximation provides a better means of understanding the calculated differential cross sections.

In the weak-coupling limit, one can define the deflection function semiclassically as the derivative of the Jeffreys-Wentzel-Kramers-Brillouin (JWKB) phase shift with respect to the angular momentum L. Within the two-channel model there are two possible charge-transfer paths, hence two deflection functions can be defined:[2]

$$\Theta_{\pm}=\Theta_{\rm av}\pm\Theta_d ,$$

where

$$\Theta_{\rm av}(L)=\frac{d\eta_1}{dL}+\frac{d\eta_2}{dL} , \\ \Theta_d(L,R_\times)=\frac{d\eta_1'}{dL}-\frac{d\eta_2'}{dL} . \tag{18}$$

In (18), η_1 and η_2 are the JWKB phase shifts obtained from the two adiabatic potentials, η_1' and η_2' are the same phase shifts obtained from the two adiabatic potentials in the region $R<R_\times$. Note that these phase shifts can be obtained from diabatic potentials if the Landau-Zener localized coupling condition holds.

In defining (18), however, the role of channel coupling $V_{12}(R)$ is absent. For the $Ne^{4+}+He$ system, this coupling cannot be neglected and thus the two deflection functions are defined from (15) using the stationary-phase approximation,

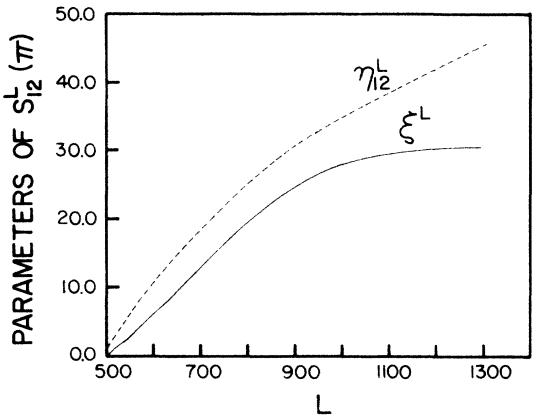

FIG. 4. Phase parameters of S_{12} for $Ne^{4+}+He$ at c.m. energy 2.3 a.u.

$$\Theta_{\pm}=\frac{d}{dL}(\eta_{12}\pm\xi) , \tag{19}$$

where η_{12} and ξ are the phase parameters of S_{12} [see Eq. (17)]. Note that $d\eta_{12}/dL$ is well approximated by $\Theta_{\rm av}$ of (18) and the difference between $d\xi/dL$ and Θ_d is a measure of the strength of the channel coupling.

The parameters η_{12} and ξ for the present system at the c.m. energy 2.3 a.u. are displayed in Fig. 4 and the corresponding deflection functions are shown in Fig. 5. Note that the slopes of η_{12} and ξ are quite close in the region $L=700-800$ and thus one of the deflection function reaches a near-zero value at the corresponding impact parameter $b_r\approx 4.5$ to produce glory scattering. This situation is quite different from the deflection functions studied previously [Fig. 4 of Ref. 7, also reproduced on the top of Fig. 6(b) here] for $C^{4+}+He$ where the two deflection functions decrease monotonically with increasing L and are nearly identical because $d\xi/dL$ is very small.

The differences in the deflection functions are due to the nature of the potential curves and the location of the crossing radius $R_\times$. For $C^{4+}+He$, $R_\times=3.1$ and for

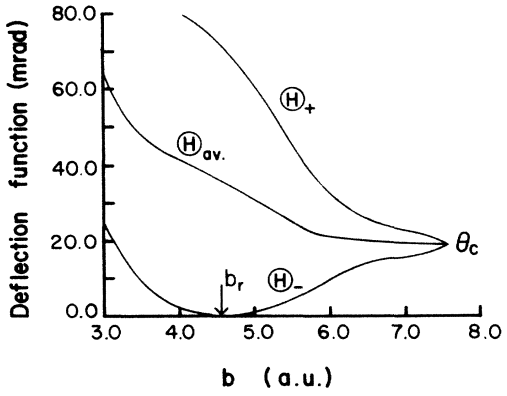

FIG. 5. Inelastic deflection function of $Ne^{4+}+He$ obtained from ξ and η_{12} of S_{12}.

$R < R_\times$, both potential curves are repulsive so that both deflection functions are monotonically decreasing with increasing L. Under this circumstance, the oscillation in the differential cross section is due completely to the Stueckelburg oscillation, or equivalently, the result of interference between the two charge-transfer "paths."

The R dependence of the potential curves near $R_\times = 7.1$ as shown in Fig. 1 for $Ne^{4+} + He$ is responsible for the behavior of the deflection functions displayed in Fig. 5. Since the crossing radius is at such a large R, the interaction potential between the two atomic centers is atomic in nature. Thus one of the potential curves, $V_{11}(R)$, is governed by an attractive polarization potential in the larger R region. This potential eventually be-

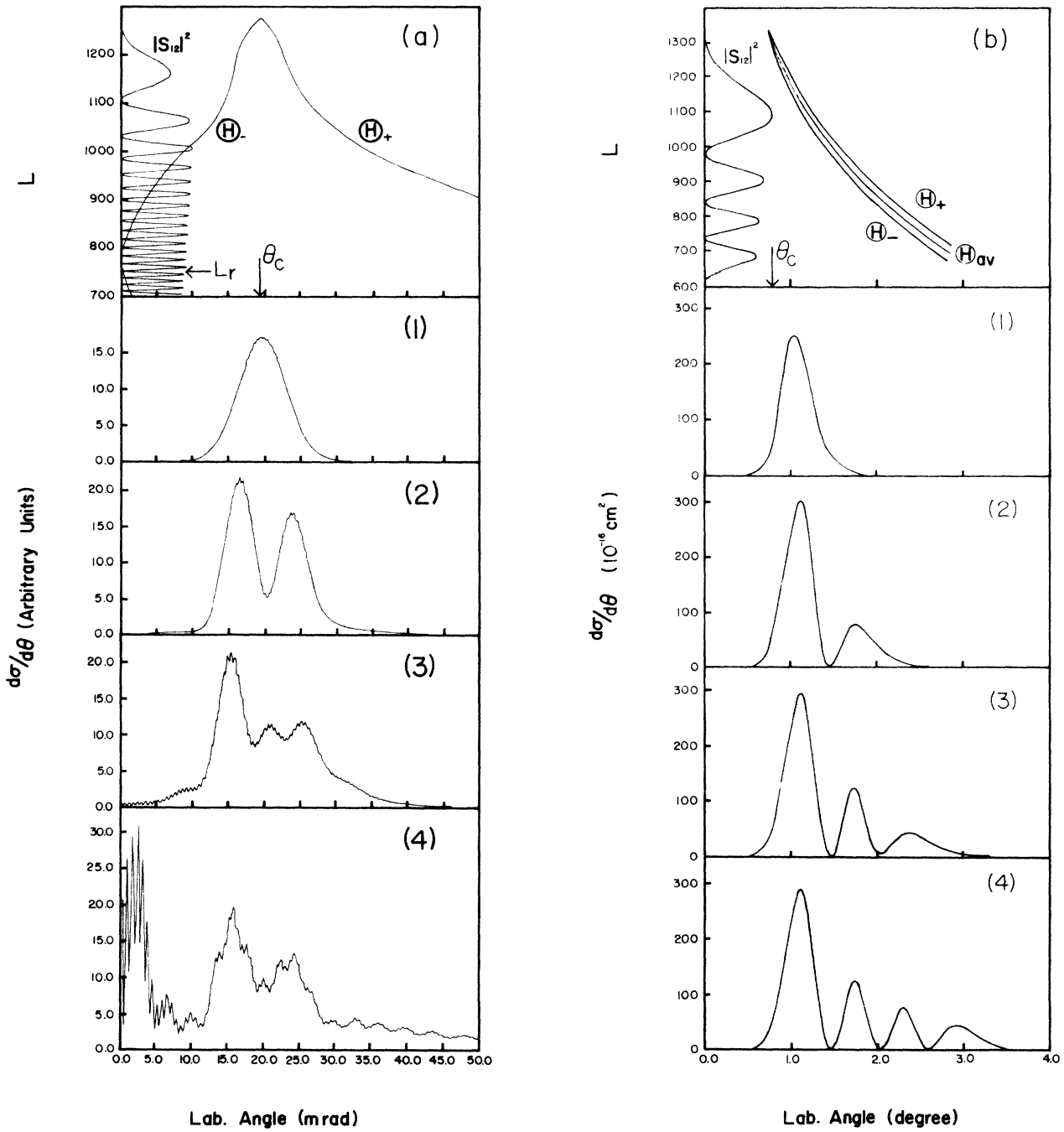

FIG. 6. Evolution of the differential cross section as different number of partial waves are summed in (15). (a) $Ne^{4+} + He$: (1) from $L_{max} = 1300$ to $L_1 = 1107$, the first minimum in $|S_{12}|^2$; (2) L_{max} to $L_2 = 1031$ (second minimum); (3) L_{max} to $L_3 = 985$ (third minimum); (4) L_{max} to L_r. (b) $C^{4+} + He$: (1) from $L_{max} = 1350$ to $L_1 = 985$ (first minimum); (2) L_{max} to $L_2 = 841$ (second minimum); (3) L_{max} to $L_3 = 736$ (third minimum); (4) L_{max} to $L_4 = 611$ (fourth minimum).

comes repulsive in the small R region as the charge cloud from the two centers begin to overlap. Since there is a change in the slope of $V_{11}(R)$, this would give rise to an inelastic rainbow. Note that the inelastic rainbow angle θ_r at $b=b_r$ (see Fig. 5) is close to zero. The other potential, $V_{22}(R)$, is almost completely repulsive in the whole region of R and thus the deflection function is monotonically decreasing with increasing L. At small impact parameters, since the inner turning point is far away from $R_\times$, this results in fast Stueckelberg oscillations.

These deflection functions allow us to interpret the oscillatory structures in the calculated differential cross sections; the forward peaking is due to the glory phenomenon, hence the fast oscillation in the forward angle is the supernumerary rainbow oscillations. By examining the area enclosed by the deflection functions, the Stueckelberg oscillations can be identified. Because θ_r, the rainbow angle, and θ_c, the angle corresponding to $b=b_{\max}$, are well separated, the oscillation is a mixture of Stueckelberg and rainbow oscillations.

There is also an interesting difference in the relation

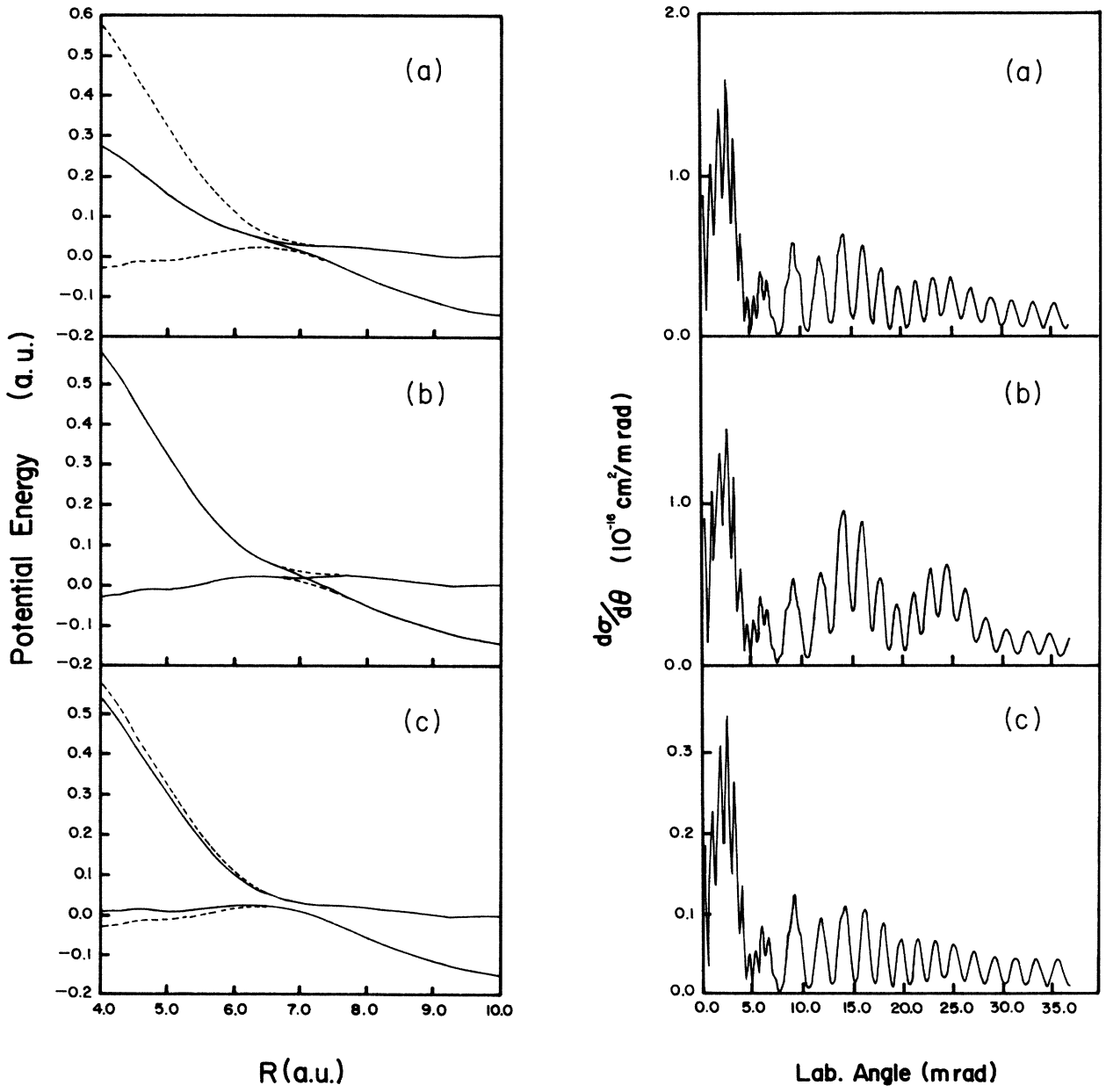

FIG. 7. Differential cross sections obtained by using different diabatic potentials (solid curve) which were transferred from the same adiabatic potentials (dashed curve) but different channel coupling strengths. (a) The Demkov-type scattering, (b) the Landau-Zener type of scattering, (c) the noncrossing type scattering. The scattering energy is 380 eV. Note that the major features of the differential cross sections are quite similar in all three cases.

between the scattering angle and the range of L's contributing to the sum of (15) for the two systems. We define the relation to be "local" if there is a definite range of L's responsible for the structure at a certain range of angles. Otherwise, the relation is "nonlocal." In this sense, $C^{4+}+He$ is a local case and $Ne^{4+}+He$ is a nonlocal case. This is illustrated in Fig. 6.

Figure 6(a) illustrates the case for $Ne^{4+}+He$. On the top frame of this figure, the deflection functions and $|S_{12}|^2$ are also shown. The next four frames show the structure of the differential cross sections as more and more partial waves are added to the summation in (15). If we add L from $L_1=1107$, where $|S_{12}|^2$ has the first minimum (see the top frame), to $L_{\max}=1300$, we obtain a broad peak around θ_c. As we add more partial waves, say from $L_1=1031$, where $|S_{12}|^2$ has the second minimum to $L_{\max}$, the broad peak splits into two peaks on each side of θ_c. [The number of peaks n in the differential cross section is related to the phase ξ of S_{12} through $\xi(L_2)-\xi(L_1)=n\pi$.] As more and more partial waves are added, say from L_r (corresponding to b_r) to $L_{\max}$, we begin to see the profile of slow oscillations (the bottom frame). If partial waves smaller than L_r are added, the final fast Stueckelberg oscillations begin to appear. Therefore, in this case it is not possible to attribute a certain range of L to the structure of differential cross sections in a local angular region.

The situation is much simpler in $C^{4+}+He$. A similar partial sum over L indicates that as more small L's are included, the structures at small angles do not change; only that new features appear at larger angles. Thus it is possible to relate on a one-to-one basis the oscillatory structures in $|S_{12}|^2$ with respect to L to the structures in the differential cross sections with respect to θ. This situation is considered to be local.

We close this section by remarking that experimental observations are unable to determine definitely whether the forward peaking in the differential cross section is a glory scattering or that the peak occurs at a finite angle. The model potentials chosen here is such that the peak is a glory scattering.

IV. DISCUSSION

The model potentials chosen to fit the experimental differential cross-section data are not unique. Utilizing a semiclassical argument, it has been shown[12] that the transition amplitude does not depend upon the individual V_{ij} $(i,j=1,2)$, but rather upon the ratio $(V_{11}-V_{22})/2V_{12}$ only. Therefore, different sets of diabatic potentials could give almost identical scattering matrices and differential cross sections in a limited energy region.

There is less freedom in constructing model potentials in the adiabatic representation than in the diabatic representation. For a fixed potential $\underline{V}^a$, any change in the coupling P_{12} forces the change in each V_{ij} as well as a change in the ratio $(V_{11}-V_{22})/2V_{12}$ (this ratio is related to P_{12} through the diabatic transformation angle ε). However, changing P_{12} alone does not change the features in $\sigma(\theta)$ significantly except the absolute magnitudes. To illustrate this point, we display in Fig. 7 several differential cross sections obtained with fixed adiabatic potential curves with various coupling terms. The coupling strength is measured in terms of the maximum transformation angle $\varepsilon_{\max}$ which is equal to 1.266 for the potentials shown in Fig. 2. The diabatic potentials for each case are shown in Fig. 7 by solid lines.

Case (a): P_{12} is reduced by a constant factor such that the $\varepsilon_{\max}\simeq\pi/4$. Thus V_{11} and V_{22} are nearly equal when $R<R_\times$. This is the Demkov-type crossing.[13]

Case (b): P_{12} is very narrow and $\varepsilon_{\max}=\pi/2$. Here the diabatic coupling is significant only near $R=R_\times$. This is the Landau-Zener type coupling.

Case (c): P_{12} is small and $\varepsilon_{\max}<\pi/4$. The two diabatic potentials do not cross each other and this is the "noncrossing" scattering.

From Fig. 7, we note that the features of the differential cross sections are very similar in all three cases, despite that the diabatic potentials are very different. Thus it is easier to model the potentials in the adiabatic representation to extract the dominant features in the differential cross sections and then fit P_{12} to obtain absolute cross sections.

In summary we have shown in this paper that by approximating the charge-transfer reaction (1) as a two-channel problem it is possible to adjust the empirical potentials so that a quantal calculation would reproduce the major features of the measured differential cross sections. The oscillatory structures in the experimental data were attributed to the envelope of the unobserved fast oscillations, the latter being due to the combined effect of rainbow scattering and of Stueckelberg oscillations. This interpretation is different from the one for the oscillation in the previously studied system $C^{4+}+He$. Semiclassical analysis is used to aid the understanding of the origin of these differences.

We remark that the model potentials deduced here are capable of explaining experimental results. This is by no means implying that calculated *ab initio* potential curves will lie on top of the present ones because of the many degrees of freedom in the fitting of potential curves to obtain experimental differential cross sections. Nevertheless, the model potentials deduced here do allow us to analyze the major features of the observed structures in the differential cross sections. In this respect, *ab initio* calculations of potential curves for this system are highly desirable.

ACKNOWLEDGMENTS

The authors gratefully acknowledged a discussion with C. L. Cocke and M. Kimura. This work is partly supported by the U.S. Department of Energy (Office of Energy Research, Division of Chemical Sciences).

*Current address: Fakultät für Physik, Hermann Herder Strasse 3, D-7800 Freiburg, West Germany.

[1]See, for example, H. Massey, *Atomic and Molecular Collision* (Taylor and Francis, London, 1979).
[2]R. E. Olson and F. T. Smith, Phys. Rev. A **3**, 1607 (1971).
[3]N. Shimakura, H. Inouye, and T. Watanabe, J. Phys. B **17**, 2687 (1984).
[4]T. G. Heil, S. E. Butler, and A. Dalgarno, Phys. Rev. A **23**, 1100 (1981).
[5]P. Roncin, M. N. Gabori, M. Barat, and H. Laurent, Europhys. Lett. **3**, 53 (1987).
[6]C. Gaussorgues, C. Le Sech, F. Masnou-Seeuws, R. McCarroll, and A. Riera, J. Phys. B **8**, 235 (1975).
[7]L. N. Tunnell, C. L. Cocke, J. P. Giese, E. Y. Kamber, S. L. Varghese, W. Waggoner, Phys. Rev. A **35** 3299 (1987).
[8]W. Waggoner, C. L. Cocke, L. N. Tunnell, C. C. Havener, F. W. Meyer, and R. A. Phaneuf (unpublished).
[9]A. Barany, H. Danard, H. Cederquist, P. Hvelpund, H. Knudsen, J. O. K. Pedersen, C. L. Cocke, L. N. Tunnell, W. Waggoner, and J. P. Giese, J. Phys. B **19**, L427 (1986).
[10]J. Tan, C. D. Lin, and M. Kimura, J. Phys. B **20**, 91 (1987).
[11]B. Johnson, J. Comput. Phys. **13**, 445 (1973).
[12]T. Dinterman and J. Delos, Phys. Rev. A **15**, 463 (1977).
[13]Yu. N. Demkov, Sov. Phys.—JETP **18**, 138 (1964).